Computer simulations suggest that prostate enlargement due to benign prostatic hyperplasia mechanically hampers prostate cancer growth

Guillermo Lorenzo[a,1], **Thomas J. R. Hughes**[b], **Pablo Dominguez-Frojan**[c], **Alessandro Reali**[d], **and Hector Gomez**[c]

[a]Departamento de Matemáticas, Universidade da Coruña, Campus de Elviña s/n, 15071 A Coruña, Spain; [b]Institute for Computational Engineering and Sciences, The University of Texas at Austin, 201 East 24th Street, C0200, Austin, TX 78712-1229, USA; [c]School of Mechanical Engineering, Purdue University, 585 Purdue Mall, West Lafayette, IN 47907, USA; [d]Department of Civil Engineering and Architecture, University of Pavia, via Ferrata 3, 27100 Pavia, Italy

This manuscript was compiled on July 13, 2018

Prostate cancer and benign prostatic hyperplasia are common genitourinary diseases in aging men. Both pathologies may coexist and share numerous similarities, which have suggested several connections or some interplay between them. However, solid evidence confirming their existence is lacking. Recent studies on extensive series of prostatectomy specimens have shown that tumors originating in larger prostates present favorable pathological features. Hence, large prostates may exert a protective effect against prostate cancer. In this work, we propose a mechanical explanation for this phenomenon. The mechanical stress fields that originate as tumors enlarge have been shown to slow down their dynamics. Benign prostatic hyperplasia contributes to these mechanical stress fields, hence further restraining prostate cancer growth. We derived a tissue-scale, patient-specific mechanically-coupled mathematical model to qualitatively investigate the mechanical interaction of prostate cancer and benign prostatic hyperplasia. This model was calibrated by studying the deformation caused by either disease independently. Our simulations show that a history of benign prostatic hyperplasia creates mechanical stress fields in the prostate that hamper prostatic tumor growth and limit its invasiveness. The technology presented herein may assist physicians in the clinical management of benign prostate hyperplasia and prostate cancer by predicting pathological outcomes on a tissue-scale, patient-specific basis.

prostate cancer | benign prostatic hyperplasia | mathematical oncology | patient-specific | isogeometric analysis

Despite its small size and supporting role in the male genitourinary system, the prostate is the site of two major pathologies in older men: prostate cancer (PCa) and benign prostatic hyperplasia (BPH) (1). PCa is almost always an adenocarcinoma, a form of cancer that originates in epithelial tissues with glandular organization, for instance, the prostatic tissue in charge of producing certain substances of semen. Currently, PCa is the second most common cancer and the fifth leading cause of death from cancer in men worldwide, with estimated 1.1 million new cases and 307,000 deaths in 2012 (2). PCa is usually diagnosed and treated when it is still localized within the prostate (1). The majority of PCa cases originate in the peripheral zone (PZ) of the prostate (70%), but PCa can also arise in the transition zone (20%) and in the central zone (10%). BPH consists of the pathological enlargement of the prostate with age, with a prevalence increasing from 50% in men in their fifties to about 70% in men in their seventies (3). This condition may arise in the transition zone or the periurethral glands (1). The growing tissue may obstruct urinary and ejaculatory flow, hence causing bothersome lower-urinary tract symptoms. As BPH does not develop in the PZ, the glandular prostate is segmented into two zones in radiological studies: the PZ and the central gland (CG), which contains the central, transition, and periurethral zones (1, 4, 5). The CG has a larger and denser stromal component that becomes more compact during BPH, which results in an overall lower signal intensity in T2-weighted magnetic resonance (MR) images. However, the signal intensity of the CG is usually rather heterogeneous due to the varying proportions of stromal and glandular hyperplasia (1, 4–7).

Beyond anatomical location, BPH and PCa possess other similarities (1, 8, 9). At the epidemiological level, both diseases affect older men, have increasing incidence with age, and frequently coexist in the same patient. These pathologies may induce lower urinary tract symptoms and increase serum levels of Prostatic Specific Antigen (PSA), a prostate activity biomarker used in PCa diagnosis and staging. Additionally, PCa and BPH share some genetic alterations, are hormone-dependent, have been correlated with prior inflammation, and might be part of the metabolic syndrome. Despite the evidence suggesting links between PCa and BPH, the relationship between these diseases has been under continuous debate in

Significance Statement

Benign prostatic hyperplasia (BPH) is a common disease in aging men that causes the prostate to enlarge progressively. Men with larger prostates tend to harbor prostatic tumors with more favorable features. The underlying mechanisms that explain this interaction between BPH and prostate cancer are largely unknown. Here, we propose a feasible theory. The mechanical stresses generated during tumor growth are known to slow down its dynamics. BPH creates increasingly intense mechanical stress fields in the prostate over time. Hence, BPH mechanically hampers the growth of prostate cancer. We extended our mathematical model of prostate cancer growth to include the mechanical deformation of the prostate under BPH and prostate cancer and run a series of computer simulations to explore our theory.

G.L and H.G. conceived and designed the study, developed and implemented the mathematical model, and wrote the paper; G.L. performed the numerical simulations; G.L., T.J.R.H., A.R., and H.G. structured and analyzed the results; T.J.R.H., A.R. and H.G. supervised the study; G.L., P.D.F., and H.G. developed the technology to construct the prostate mesh. All authors reviewed and approved the final version of the manuscript.

H.G., T.J.R.H., and G.L. are listed as coinventors in a patent application that has been filed by The University of Texas at Austin. The invention leverages part of the technology presented in this paper.

[1]To whom correspondence should be addressed. E-mail: guillermo.lorenzo@udc.es

the medical community due to the existence of contradictory studies and the scarcity of research thoroughly confirming the proposed hypothetical links (8, 9). Gaining knowledge about the connection between PCa and BPH would challenge the current clinical standards and potentially enhance treatment and prevention of both diseases.

The biopsy detection rate of PCa in large prostates is known to be lower than in small prostates (10–12). This low detection rate has been attributed to various artifacts, such as sampling errors and a biopsy selection bias in patients with increasing PSA, possibly caused by BPH (10, 13, 14). However, it appears that neither increasing sampling nor using more advanced medical imaging to perform biopsy has leveled the detection rate across prostate volume groups (11, 12, 15, 16). Recent studies on large series of radical prostatectomy specimens show that tumors arising in larger prostates present favorable pathological features, such as lower aggressiveness measured with the Gleason Score (1), smaller tumor volume, and lower risk of extraprostatic extension or seminal vesicle invasion (10, 17–21). These studies provide solid evidence to suggest that large prostates may exert a protective effect against PCa, but the underlying mechanisms are not known.

Here, we propose a mechanical explanation for this phenomenon: BPH exerts an inhibitory effect on PCa growth due to the accumulation of mechanical stress. The rapid overproliferation of cancerous cells leads to high cell densities in their confined microenvironment within the harboring tissue. As a result, tumors develop a high compressive hydrostatic stress state in their interior and exert outward forces as they grow. These forces deform the neighboring tissues, generating stress fields aimed at resisting the mechanical load imposed by tumor growth. This phenomenon is known as the *tumor mass effect* (22–28). In turn, these mechanical stress fields are known to exert an inhibitory effect on tumor growth both directly, by slowing down tumor dynamics, and indirectly, by deforming and collapsing the local vasculature in the tumor region. BPH creates a compressive hydrostatic stress state within the CG and outward forces that deform the PZ (1, 4, 5). Here, we show that, as the CG enlarges over time, the mechanical stress fields created by BPH intensify and reach larger values than those created by the tumor itself. Hence, BPH may also exert an inhibitory effect on PCa growth but its impact has been overlooked. Additionally, the confinement of the prostate in the pelvic area further contributes to the internal mechanical stress fields because the surrounding tissues resist the pathological deformation of this organ.

To analyze whether enlarged prostates may provide protection against PCa growth, we need to determine whether the stress induced by BPH is enough to significantly produce an inhibitory effect on PCa. This fundamentally requires a 3D, anatomically faithful, mechanical model of the prostate. The amount by which the growth rate of the tumor decreases with stress may be estimated from experiments in the literature. To perform this study, we derive a tissue-scale, patient-specific mechanically-coupled mathematical model for PCa growth and perform a series of computer simulations. The study and design of mathematical models to forecast the evolution of tumors using computer simulations has given rise to the field of mathematical oncology (29–31). These models aim at complementing the current clinical practice in oncology by assisting physicians in better estimating disease progression and designing optimal treatment schemes. In particular, several mathematical models have incorporated the tumor mass effect to improve the prediction of the growth of various types of cancers (32–38). Fig. 1 depicts the geometry of the prostate used in our simulations, which we extracted from the MR images and anatomical segmentations of a patient suffering from PCa and BPH.

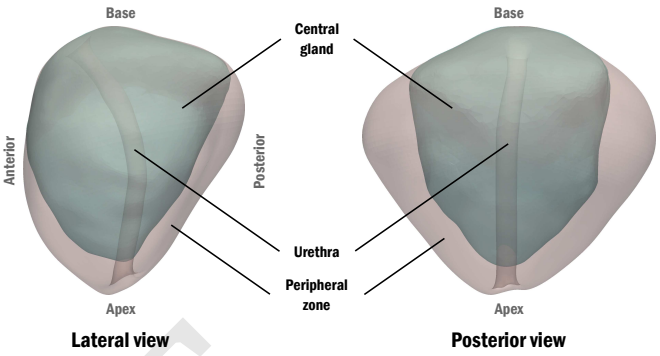

Fig. 1. Patient-specific local anatomy of the prostate. From a radiological perspective, the prostate is divided in central gland (CG) and peripheral zone (PZ). BPH takes place in the CG and most cases of PCa arise in the PZ. We extracted the geometry of the patient's prostate and CG from their corresponding segmentations provided on axial T2-weighted MR images. The volumes of the prostate, CG, and PZ at MRI date are 52.81 cc, 33.15 cc, and 19.66 cc, respectively. The major diameters of the prostate at MRI date have a length of 53.49 mm, 38.35 mm, and 52.01 mm in lateral, anteroposterior, and craniocaudal direction, respectively.

In this work, we extend our previous model of organ-confined PCa growth (39, 40) to include the equations of mechanical equilibrium and define the coupling terms between them and tumor dynamics. As organ-confined PCa growth can be seen as an evolving interface problem, we leverage the phase-field method (41) to account for the coupled dynamics of healthy and tumoral tissue. Our model also estimates PSA dynamics at tissue level by computing the serum concentrations of this biomarker produced at healthy and cancerous regions per unit volume of prostatic tissue (39). Following previous mechanically-coupled approaches (32–38), we assume that the deformation of the prostate is a quasistatic phenomenon and we model prostatic tissue as a linear elastic, heterogeneous, isotropic material. As CG is normally stiffer than PZ in older men, we set a higher Young modulus in the CG (1, 4–7, 42–45). The confinement of the prostate in the pelvic region is modeled with Winkler boundary conditions on the external surface of the organ, while free displacement is imposed along the urethra. BPH and PCa are modeled as pressure terms in the constitutive equation of the prostatic tissue acting within the CG and the tumor, respectively. Finally, the inhibitory effect of the mechanical stress fields is estimated with a global factor that slows down tumor dynamics. This coefficient depends on a measure of the loading conditions and the stored elastic energy, so we choose a combination of the Von Mises stress and the hydrostatic stress for this purpose (46). The range of values of this inhibitory factor is adjusted to match the experimental and clinical observations in previous studies of tumor growth (23–28, 32–34). See the section on Methods for more details on the model.

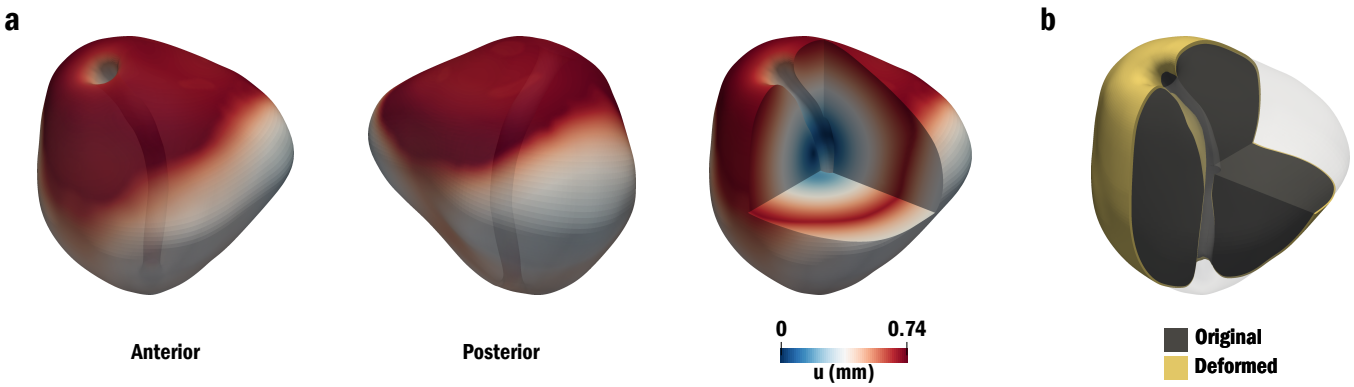

Fig. 2. Deformation of the prostate caused by BPH over 1 year. (a) Length of the displacement field vector over original anatomy at $t = 1$ year. (b) Original and deformed geometries of the prostate at $t = 1$ year.

Results

Deformation of the prostate due to BPH. Our model predicted that BPH produces the volumetric expansion of the prostate in the perpendicular direction to the CG border, as depicted in Fig. 2 and Fig. S1. The PZ was pushed outwards from the borders of the growing CG against the prostate external surface and experimented a very slight shrinkage, as the Winkler boundary conditions partially enabled outward displacement.

The extremal values of the displacements were attained at the CG borders that are closer to the external surface of the prostate. The maximum total displacement was 0.74 mm. The urethra was displaced posteriorly and its diameter was virtually unaltered.

The hydrostatic stress was compressive within the CG (-0.20 to -0.13 KPa) and negligible within the PZ (see Fig. S1). Positive hydrostatic stress appeared in thin PZ regions between the CG border and the prostate boundary, where tension accumulated as the CG expanded. The Von Mises stress was negligible within the CG, except along the urethra (0.27 to 0.53 KPa). Within the PZ, the Von Mises stress peaked near the borders of the CG (0.20 to 0.33 KPa) and decreased towards the external surface of the prostate (0.07 to 0.17 KPa), depending on the distance between them (see Fig. S1).

Deformation of the prostate due to PCa. We considered three artificial tumors placed in characteristic locations within the prostate: the basal PZ, the apical PZ, and the CG. Each tumor had ellipsoidal geometry with one semiaxis measuring 4 mm and the others 3 mm. The largest dimension was oriented in anteriorposterior direction. We selected the parameters that regulate tumor dynamics so that these tumors were aggressive and showed the typical morphologies of localized PCa: massive and fingered (39). Fig. 3 and Fig. S2 show the growth of these artificial tumors and how they deformed our patient's prostate.

All tumors started growing with the massive morphology, which is characteristic of small prostatic cancers. The PZ tumors soon adjusted their geometry to the anatomy of the patient's prostate boundary (see Fig. 3(a1-a2) at $t = 0.3$ years). Due to the reduced thickness of the PZ around the CG in our patient's prostate, these PZ tumors invaded the CG early ($t < 0.1$ years). The CG tumor took longer to reach the PZ and invade it ($t \approx 0.3$ years). As every tumor grew in size, the intratumoral nutrient concentration decreased. This shortage cued a shape instability that progressively adjusted the tumors to a fingered or lobular morphology, hence ensuring a spatial distribution of nutrient that sustained tumor growth (39). This phenomenon happened by $t = 0.4$ years for the tumor in basal PZ, by $t = 0.35$ years for the tumor in apical PZ, and by $t = 0.55$ years for the CG tumor. The shift in morphology arrested tumor growth momentarily (< 0.15 years) and even reduced the CG tumor volume by 12.2%. However, tumors grew faster and more extensively after this phenomenon.

The CG tumor grew faster and larger than the PZ tumors, whose growth rates and initial volumes were similar. Because the tumor in apical PZ underwent the change in morphology earlier, its volume was larger than the basal PZ tumor for the second half of the simulation. The final volumes of the basal PZ tumor, the apical PZ tumor, and the CG tumor were 5.43 cc, 6.82 cc, and 9.02 cc, respectively.

Tumors produced a local swelling deformation. The outermost tumoral structures produced the greatest displacements, which ranged between 0.65 and 1.15 mm and created noticeable smooth lumps on the external prostatic boundary, especially in the PZ (see Fig. 3(b1-b3), Fig. 3(c1-c3), and Fig. S2). The CG tumor barely deformed the posterior aspect of the PZ. During the shift in tumor morphology, the displacement fields redistributed and decreased globally between 23% and 31%, taking 0.3 to 0.6 years to recover during fingered growth. The urethra was displaced away from the tumor and also constricted (max. 0.44-0.75 mm), mainly in the segments circumvented by the fingered tumors.

The hydrostatic stress was compressive within the tumors, with lower values in the PZ (-0.75 to -0.33 KPa; see Fig. S2). Around the tumors, the hydrostatic stress was compressive in the PZ, with a minimum of -0.08 KPa, and tensile in the CG, with a maximum of 0.10 KPa. Maximal tensile hydrostatic stress between 0.67 and 0.88 KPa was obtained on the most constricted contours of the urethra and was accompanied by compressive values with minimum between -0.52 and -0.38 KPa on the urethral contours in perpendicular direction to the constriction. High tensile hydrostatic stress was also registered when tumors grew near the prostate external surface (up to 0.33 KPa in PZ and 0.48 KPa in CG). Far from the tumor, the hydrostatic stress was negligible.

The Von Mises stress ranged between 0.05 and 0.25 KPa inside the tumor and it was higher around the convex side of

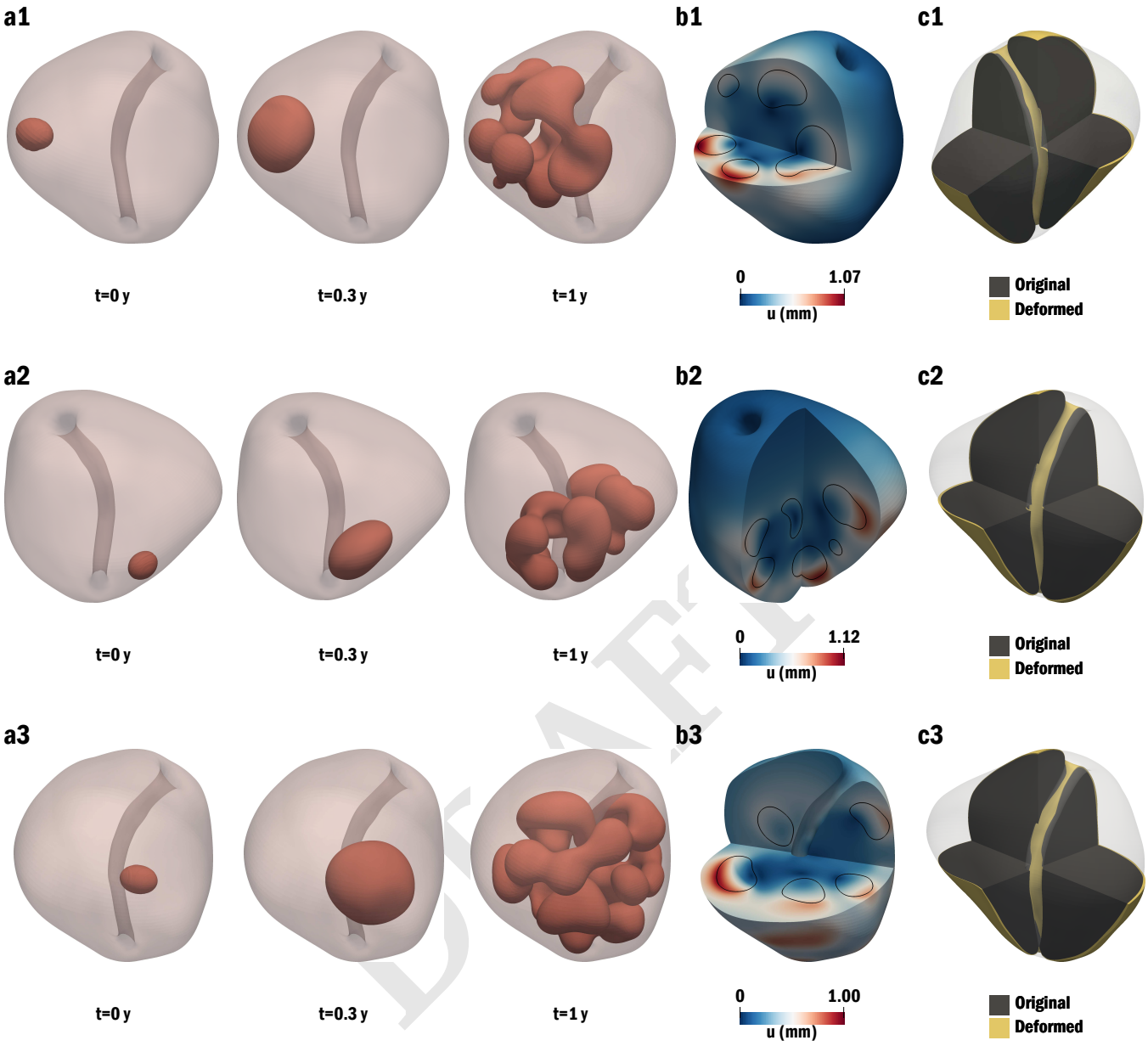

Fig. 3. Deformation of the prostate over 1 year produced by a tumor originated on basal PZ (a1-c1), apical PZ (a2-c2), and median CG (a3-c3). (a1-a3) Tumor growth over the original prostate geometry. (b1-b3) Length of the displacement field vector over original anatomy at $t = 1$ year. The contour of the tumor is depicted with black curves. (c1-c3) Original and deformed geometries of the prostate at $t = 1$ year.

the tumor borders, with values typically between 0.45 and 0.60 KPa (see Fig. S2). Maximal values of the Von Mises stress were obtained in the healthy tissue between tumor branches (0.60 to 0.70 KPa), within intricate concave regions of fingered tumors (0.60 to 0.75 KPa), within and around the tumor near the border between the PZ and the CG (0.41 to 0.87 KPa), in healthy tissue compressed by the tumor against the prostate external surface (0.50 to 0.92 KPa), and on the contour of the most constricted segments of the urethra (0.75 to 1.27 KPa). The healthy tissue enclosed by tumor branches had Von Mises stress values within the intratumoral range. Massive tumors tended to build up greater values of the Von Mises stress around them. We observed that the Von Mises stress was slightly higher and the distortion rim was thicker in the CG.

BPH hampers PCa growth. After the deformational study of the prostate under the effect of BPH and PCa to calibrate our model, we analyzed how the patient's history of BPH affected PCa growth. We ran two simulations: one without considering BPH and another including it. Fig. 4 and Fig. S3 depict the growth of the tumor in both scenarios, while Fig. 5 and Fig. S4 show the deformational states. The geometry of the patient's tumor was extracted from the same MR dataset used to obtain the prostate anatomy. We estimated the stress state of the prostate caused by years of developing BPH prior to PCa detection at the MR date, $\boldsymbol{\sigma}^0$. This information was introduced as a prestress to compute the baseline hydrostatic and Von Mises stresses in the mechanotransductive coefficient adjusting

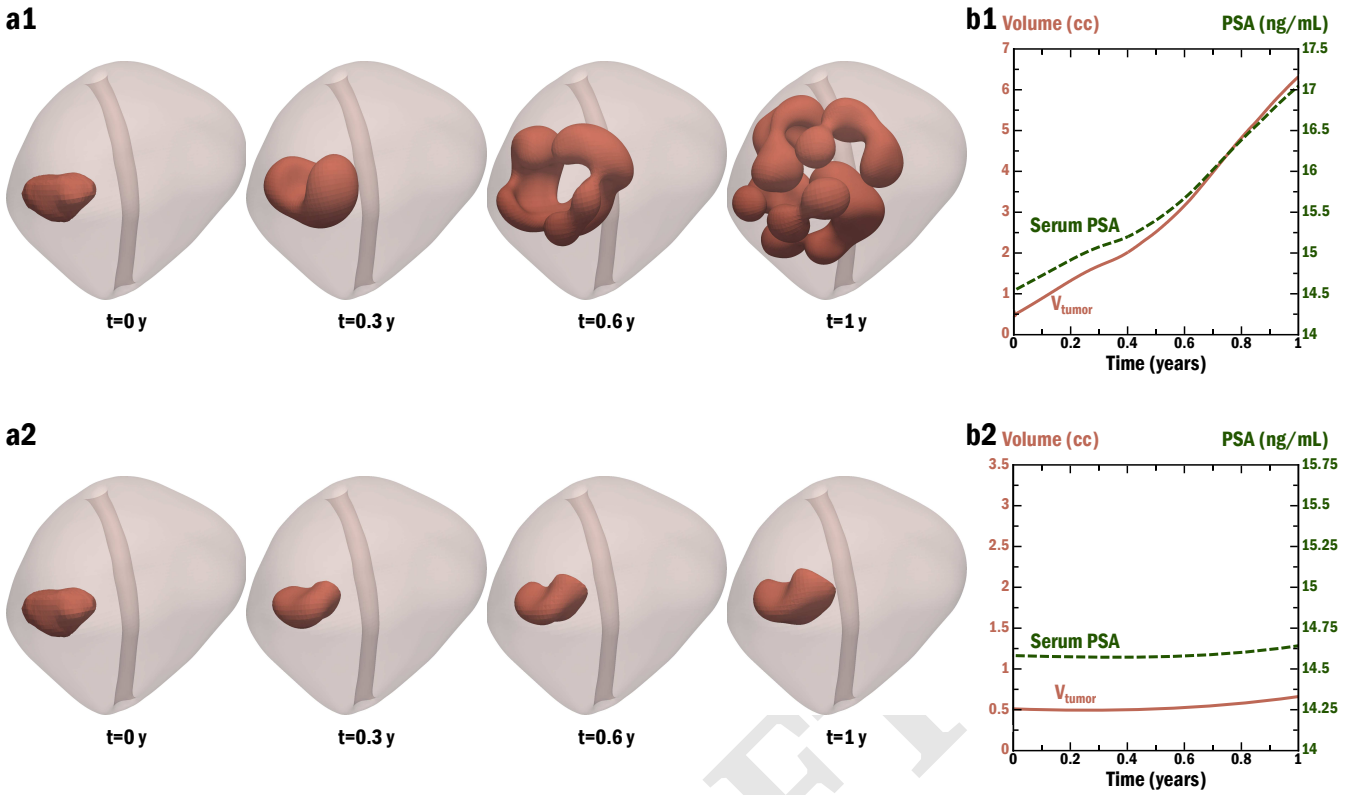

Fig. 4. Growth of the patient's tumor over 1 year without the influence of BPH (a1-b1) versus considering the patient's history of benign prostatic enlargement (a2-b2). (a1-a2) Tumor growth over the original prostate geometry. (b1-b2) Time history of tumor volume (solid line) and serum PSA (dashed line).

tumor dynamics (see the section on Methods). Hence, for this purpose, $\boldsymbol{\sigma} = \boldsymbol{\sigma}^0 + \boldsymbol{\sigma}^1$, where $\boldsymbol{\sigma}^1$ are the stresses developed since the detection of PCa at MR date.

The simulation without BPH rendered similar results to the PZ tumor cases in the previous section. The patient's tumor was located in the left basal aspect of the PZ and had a volume of 0.51 cc. Initially, this tumor grew with massive morphology, early invading the CG and progressively developing two lobes of preferential growth in the anteriorposterior direction. This geometry contributed to an early shift in morphology between $t = 0.3$ and $t = 0.4$ years, during which tumor growth was minimally slowed down. Afterwards, the tumor grew faster with fingered morphology, invading all the prostate side where it had originated from median to basal height in the craniocaudal direction.

The final volume of the tumor was 6.32 cc. The urethra was displaced anteriorly to the patient's right and the maximal constriction was 0.30 mm. The distribution and magnitude of the displacement, hydrostatic stress, and Von Mises stress fields were also analogous to their counterparts in the simulations for the PZ tumors in the previous section. The maximum total displacements were in the range 0.85-1.05 mm. The shape instability reduced displacements by 17.3% and it took until the end of the simulation for them to recover ($t \approx 0.9$).

The inclusion of the patient's history of BPH produced major changes in tumor growth and the prostate deformational state. There was no shift in morphology in this simulation. Instead, the tumor grew as a continuous mass that progressively surrounded the CG anteriorposteriorly at the basal level of the PZ. The invasion of the CG was minimal and only involved the border with the PZ. The tumor growth rate was considerably lower than in the simulation without BPH and the final volume of the cancerous mass was 0.66 cc.

BPH globally dominated the deformation of the prostate by producing a volumetric expansion. The tumor produced a local swelling deformation that was noticeable on the external surface of the PZ. The urethra was displaced posteriorly to the patient's right and its diameter was practically unchanged. The deformation of the prostate caused by this combination of BPH and PCa produced maximum global displacements between 0.86 and 1.16 mm. These values were attained on the outer region of the tumor within the PZ. On the opposite side of the cancerous mass, the displacement field created by BPH within the CG was barely modified by the presence of the growing tumor.

The patient's history of BPH produced a highly compressive hydrostatic stress field in the prostate, ranging from -2.90 to -2.20 KPa within the CG and from -0.60 to -0.25 KPa within the PZ. The tumor contributed to increase the hydrostatic stress in the PZ, reaching minima between -0.95 and -0.70 KPa within the tumor and between -3.70 and -2.90 KPa next to the CG border. BPH led to the accumulation of compressive stress all around the urethra (-6.20 to -3.00 KPa) and tensile stress at the PZ tissue in the vicinity of the border between PZ and CG nearby the prostate external boundary (2.00 to 5.90 KPa).

The accumulated deformation by BPH also raised the Von Mises stress in the whole prostate. Within the CG, it ranged from 0.10 KPa at inner tissue, far from both the urethra and the external prostatic boundary, to higher values between 1.30

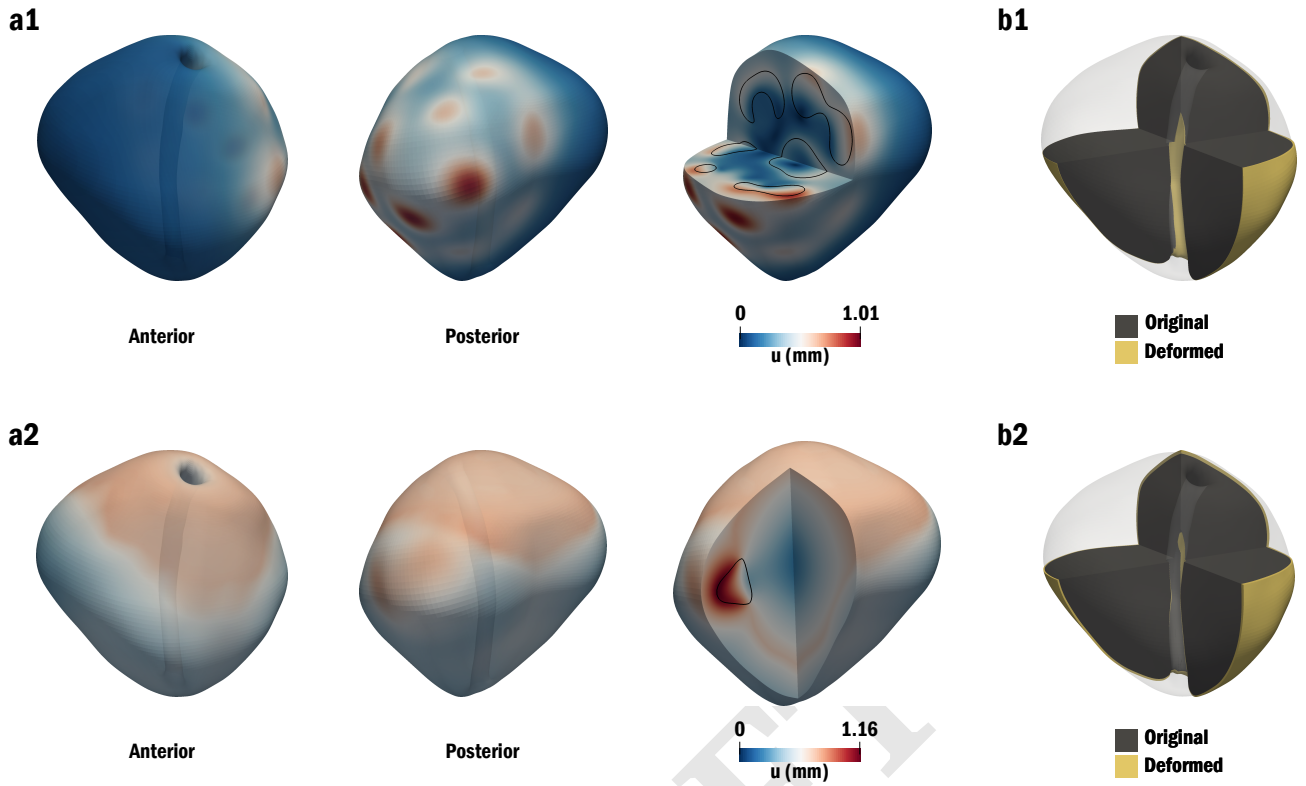

Fig. 5. Deformation of the prostate over 1 year produced by the patient's tumor without the influence of BPH (a1-b1) versus considering the patient's history of benign prostatic enlargement (a2-b2). (a1-a2) Length of the displacement field vector over original anatomy at $t = 1$ year. The contour of the tumor is depicted with black curves. (b1-b2) Original and deformed geometries of the prostate at $t = 1$ year.

and 1.80 KPa on the CG border. Within the PZ, the Von Mises stress was maximal on the CG surface, from 3.50 to 5.00 KPa. The values of the Von Mises stress then decreased toward the prostate exterior boundary, where they ranged from 1.00 to 2.50 KPa. The tumor locally increased the Von Mises stress, reaching 1.70 KPa to 2.65 KPa on its outer lateral convex border within the PZ, within the tumor near its concave border, and surrounding the tumor tips in craniocaudal direction. The intratumoral values were between 1.50 and 2.20 KPa. The maximum Von Mises stress was observed along the urethra, especially along the anterior and posterior walls, ranging from 3.00 to 8.00 KPa.

Discussion

In this work, we provide a mechanical explanation to understand why large prostates may exert a protective effect against PCa (10, 17–21). Using computer simulations based on a mechanically-coupled mathematical model of organ-confined PCa, we show that a patient's history of BPH creates a deformational state that hampers tumor growth. Our results show that BPH promoted a highly compressive hydrostatic stress state within the CG and distorted the whole prostate, especially the PZ, hence increasing the Von Mises stress. The combination of this deformational state with the mechanical stress fields created by PCa hindered tumor growth, which showed a favorable pathological evolution characterized by a slow growing rate and the lack of invasive demeanor. This resulted in a smaller tumor volume, which is more likely to have lower Gleason Score (47, 48) and hence be less aggressive. PCa was unable to grow beyond a certain thickness that would have motivated a shape instability towards a more invasive morphology, which would facilitate invasion of seminal vesicles or extracapsular extension. Instead, the deformational state of the prostate controlled the tumoral volume and only permitted its development along the less distorted and stressed directions. Increasing the Von Mises stress caused by both BPH and PCa in the prostatic tissue between the tumor and the prostate external boundary would also contribute to prevent the tumor from escaping the prostate.

These results advise performing a comprehensive examination of the prostate in men without PCa before prescribing BPH treatments or drugs aimed at reducing the CG volume. Likewise, our results recommend a close follow-up of those PCa patients receiving these sorts of BPH drugs. Otherwise, the prostate volumetric decrease could hazardously lower the mechanical stress fields created by BPH and hence reduce their mechanical restraint on PCa growth. Indeed, this could partially explain the higher proportion of more aggressive cancers in the finasteride arm of the Prostate Cancer Prevention Trial (49), arguably the most controversial result of this milestone study on chemoprevention of PCa (14, 18–20). Our research also calls for new courses of treatment alleviating BPH symptoms while maintaining a significant stress level within the prostate for protection against PCa. In the future, we intend to address this issue by extending our model to incorporate the effect of drugs causing a prostate volume decrease, such as dutasteride and finasteride (1, 49).

In order to calibrate and test our mechanically-coupled mathematical model, we also studied the deformation of the

prostate under the development of BPH and PCa. Overall, our results in terms of displacements and deformational features for BPH and PCa agree with previous studies in the medical literature (1, 42, 50). BPH produced the volumetric expansion of the prostate, with slightly higher displacements craniocaudally and anteriorposteriorly at the basal level. The compression of the PZ dampened the displacement fields elsewhere. Simulation of BPH during several years would also produce the constriction of the urethra, as cued by the high Von Mises stress along its trajectory.

PZ tumors deformed the outer posterior surface of the prostate, which would be noticed by a physician during a digital rectal examination (1). The CG tumor produced lower displacements and a uniform and subtle deformation on the posterior region of the prostate boundary. This is a common difficulty to detect CG cancers during digital rectal examination. The constriction of the urethra along the segments circumvented by the tumor is likely to produce lower urinary tract symptoms. Even though the displacements decreased after the shape instability, the volumes of the prostate, the CG, and the PZ were barely modified because the tumor grew faster with the fingered morphology. Consequently, milder displacement fields expanded over a broader volume of the prostate. PZ tumors grew slower because they accumulated higher compressive stress and the PZ was globally more distorted when the tumor grew against the prostate external surface and the CG border. PZ tumors adapted their shape to overcome those obstacles, favoring tumoral geometries that also anticipated the shape instability. We also observed that our model correctly reproduced the mechanical stress fields induced by a growing tumor as previously described in the literature (22–28).

We think that our model could be exploited to improve the current technologies for deformable registration of medical images (42) by providing a theory for the evolution of BPH and PCa. The resulting algorithms would be of much interest for several applications within the clinical management of PCa on a tissue-scale, patient-specific basis, such as the accurate follow-up of tumor growth during active surveillance or the precise planning of surgery and other treatments (39). Such technology could also help to detect PCa based on the deformation of the prostate boundaries and the internal borders between prostatic regions (44, 51). Additionally, it could guide biopsies to better stage and diagnose PCa. Comparing the predictions of the model with new images and clinical data could also help to discern whether the tumor is progressing towards a more malignant behavior and to make clinical decisions accordingly (39).

However, our model presents some limitations that we plan to address in forthcoming studies. Our anatomic model of the prostate would benefit from a more precise segmentation of the internal prostatic zones accompanied by patient-specific mechanical characterization. Likewise, a spatially varying definition of Winkler conditions attending to the different tissues and organs surrounding the prostate would contribute to render more accurate predictions. Our model would also benefit from a more accurate formulation for BPH (52–54) as well as for tumor growth and deformation (26, 33, 35, 36, 38). The mechanotransductive term to adjust tumor dynamics can be refined, for instance, by testing alternative formulations or differentiating how mechanical stress affects tumor mobility, proliferation, and apoptosis (25, 27, 33). A poroelastic description of PCa growth would also help to study the effect of mechanical deformation on nutrient transport (26). This approach holds the potential to accurately investigate the heterogeneity of intratumoral metabolism or test patient-specific drug administration to the tumor *in silico*. To gain further knowledge on the mechanisms of PCa growth using our model, we believe it would be valuable to investigate the mathematical properties of the equations comprising it, for example, analyzing solvability conditions, characterizing parameter spaces, and studying the well-posedness of the problem.

Linear elasticity is a widely accepted mechanical paradigm in tumor growth models (32–38), which provided a simple mechanical framework for this study. We acknowledge that linear elasticity is an acceptable simplification for studies featuring small strains and rotations and that the values of strains in the simulations depicted in Figs. 3 - 5 are slightly outside the admissible limits for linear elasticity in a few localized regions along the tumor interface. Additionally, the prestress $\boldsymbol{\sigma}^0$ is just a gross estimate of the stress state in the prostate due to the history of BPH previous to PCa detection at MR. However, we are only using the stresses as a means to compute the mechanotransductive factor to adjust tumor dynamics (see the section on Methods). This study also features other major sources of uncertainty beyond linear elasticity, such as prostate and tumor segmentation, the PCa model itself, or the aforementioned boundary conditions on the prostate. Nevertheless, our predictive simulations still qualitatively reproduce the inhibiting effect on tumor growth caused by the tumor mass effect and a history of BPH prior to PCa detection. Additionally, our simulations reproduce physically representative deformations caused by tumor and BPH growth phenomena. In the future, to overcome the limitations of linear elasticity and obtain more accurate values of displacements and stresses we plan to account for geometric nonlinearity and investigate alternative constitutive equations for the prostate (28, 46, 55, 56), which typically involve a larger set of elastic parameters that are not easy to estimate on a patient-specific basis.

The efforts to shed light on the potential relationships between BPH and PCa have pointed out promising correlations and mechanisms of interaction (1, 8, 9). The ensuing research to validate them could greatly benefit from mathematical modelling in order to organize, comprehend, and provide a solid theory to sustain these new discoveries and guide future steps (29–31, 39). In this paper, we exemplify the scope of this approach by demonstrating that BPH builds up a deformational state that hinders the growth of prostatic tumors, which end up showing more favorable pathological features (10, 17–21). Future research spans technologies ranging from the deformable registration of medical images of the prostate to the accurate prediction of tissue-scale, patient-specific BPH evolution and PCa outcomes. However, further validation using longitudinal series of clinical data is required to corroborate our theory before addressing these challenging applications.

Materials and Methods

Patient data. Anonymized patient data were obtained from the public repository for PCa imaging data at the Initiative for Collaborative Computer Vision Benchmarking website (http://i2cvb.github.io/)

(57). Institutional review board approval and informed consent were not required for this study. We used the multiparametric MR image dataset obtained with a 3.0 Tesla Siemens Magnetom Trio TIM scanner (Erlangen, Germany). Patient cohort description and details on data acquisition have been previously described (58). For each biopsy-confirmed patient, this database includes T2-weighted MR images, dynamic contrast enhanced MR images, diffusion weighted MR images, MR spectroscopic images, apparent diffusion coefficient maps, and the segmentations of the prostate, the PZ, the CG, and the tumor by an experienced radiologist. For this research, we selected a patient aged 54 years at MR date who had a large prostate of 52.81 cc harboring a localized tumor in the PZ.

Mathematical model. Our modeling philosophy aims at developing tumor growth models based on key phenomena and featuring a limited number of representative parameters (30). This approach holds the potential for precise heterogeneous parameterization using available longitudinal clinical and imaging data from patients, and has proven successful in reproducing and predicting various types of tumor growth (30, 32–34). As a preliminary step in this direction, here we developed a mechanically-coupled model for patient-specific, organ-confined PCa growth and we leveraged it to perform a study on the mechanical interaction between PCa and BPH using literature data for parameter calibration.

Our model is described by the following equations:

$$\frac{\partial \phi}{\partial t} = M\left(D_\phi \Delta\phi - \frac{1}{\tau}\frac{\mathrm{d}F(\phi)}{\mathrm{d}\phi} + \chi s - A\phi\right) \quad [1]$$

$$\frac{\partial s}{\partial t} = D_s \Delta s + S - \delta\phi - \gamma_s s \quad [2]$$

$$\frac{\partial p}{\partial t} = D_p \Delta p + \alpha_h(1-\phi) + \alpha_c\phi - \gamma_p p \quad [3]$$

$$\boldsymbol{\nabla}\cdot\boldsymbol{\sigma} = \mathbf{0} \quad [4]$$

Eq. (1)-Eq. (3) come from our previous theory of organ-confined PCa growth (39, 40). Eq. (1) models tumor dynamics using the phase-field method (41). The order parameter ϕ takes values from 0 in healthy tissue to 1 within tumoral regions, showing a thin diffuse interface in between. $F(\phi) = 16\phi^2(1-\phi)^2$ is a double-well potential, which enables the stable coexistence of healthy and cancerous tissue in our model. The last two terms in Eq. (1) describe nutrient-driven growth and apoptosis (i.e., programmed cell death), respectively. We consider that tumor growth is driven by a generic nutrient s that follows reaction-diffusion dynamics in Eq. (2). The reactive terms in Eq. (2) are the nutrient supply, the consumption of nutrient by the tumor, and a natural decay, respectively. Eq. (3) describes the reaction-diffusion dynamics of tissue PSA p, defined as the serum PSA concentration leaked to the bloodstream per unit volume of prostatic tissue (39). In this equation, we consider that healthy and cancerous tissue produce p at rates α_h and α_c, respectively, and the last term is a natural decay.

The mechanical stress fields generated by a growing tumor have been shown to slow down its dynamics (23–28). Previous clinically-oriented, mechanically-coupled models of tumor growth have incorporated this phenomenon by means of a coefficient that exponentially decreases cell mobility or net cell proliferation as mechanical stress fields intensify (30, 32–34). Following a similar strategy, in Eq. (1) we modeled the mechanically-induced inhibition of tumor growth throughout coefficient M, which we define in Eq. (5). Mechanical stress can be decomposed as the sum of hydrostatic stress σ_h (defined in Eq. (6)), which tends to change the volume of the stressed body, and deviatoric stress, which tends to distort it (46). The Von Mises stress σ_v (46) (defined in Eq. (7)) is a good measure of the distortional strain energy around the tumor that has been widely adopted in mechanically-coupled models (32–34). However, σ_v is insensitive to hydrostatic stress, which better describes the natural stress state within a growing region of tissue, such as a tumor or the CG developing BPH (23, 24, 26). Hydrostatic stress is also bound to increase globally during these growth processes because the prostate is a confined organ (1). Therefore, we propose to combine σ_v and the hydrostatic stress σ_h (46) in the definition of M following a similar approach to multiaxial stress-based failure criteria:

$$M = e^{-\beta_1(\sigma_v + \beta_2|\sigma_h|)}, \quad [5]$$

where

$$\sigma_h = \frac{1}{3}\boldsymbol{\sigma} : \mathbf{I} = \frac{1}{3}\left(\sigma_{11}+\sigma_{22}+\sigma_{33}\right), \quad [6]$$

$$\sigma_v = \Big(\sigma_{11}^2+\sigma_{22}^2+\sigma_{33}^2-\sigma_{11}\sigma_{22}-\sigma_{22}\sigma_{33}-\sigma_{33}\sigma_{11} +3\left(\sigma_{12}^2+\sigma_{23}^2+\sigma_{13}^2\right)\Big)^{1/2}, \quad [7]$$

σ_{ij} with $i,j = 1,2,3$ are the components of the stress tensor $\boldsymbol{\sigma}$, $\mathbf{I}$ is the second order identity tensor, and β_1 and β_2 are constants that were adjusted to match the experimental and clinical results of previous studies on tumor growth (23–28, 32–34). We use the absolute value of the hydrostatic stress because both growth-induced compressive and tensile solid stress have been shown to hamper tumor dynamics at tissue scale *in vivo* (23, 24).

We assume that PCa and BPH show sufficiently slow rates (1) to neglect the inertial effects in the deformation of prostatic tissue. Hence, Eq. (4) describes mechanical equilibrium as a quasistatic process. Linear elasticity has been widely accepted to model mechanical equilibrium in living tissue subjected to slow processes over short time scales ($t \sim 1$ year) (32–38, 46). Hence, this paradigm provides a simple mechanical framework to compute the stresses in Eq. (5) and perform our qualitative study on the mechanical influence of BPH on PCa. The prostate is an histologically heterogeneous organ: while the CG has a higher and denser stromal component, the PZ has more abundant glandular elements with sparsely interwoven smooth muscle (1, 5, 6). Benign enlargement of the prostate tends to make the CG denser and more compact (1, 7). Therefore, the CG is normally stiffer than PZ in patients with PCa and/or BPH (42–45). The growing tumor induces an internal compressive hydrostatic stress and exerts outward forces acting on the tumor border (22–24), so we modeled the tumor mass effect as

$$p_{tumor} = -\kappa\phi. \quad [8]$$

This assumes that κ is a constant compressive pressure, which is admissible over short simulation times (32–34, 36, 37). Volumetric growth due to BPH is usually modeled with an exponential function, but the slow growth rates justify a linear approximation over periods $\Delta t \sim 1-10$ years (52–54). Hence, we modeled BPH as a linearly-growing pressure acting only on the CG:

$$p_{BPH} = -K\varrho\frac{g\Delta t}{V_{MRI}}\mathcal{H}_{CG}(\mathbf{x}), \quad [9]$$

where K is the bulk modulus, g is the estimated linear volumetric growth rate of the prostate due to BPH at MR date, V_{MRI} is the volume of the prostate as measured on T2-weighted MRI, Δt is the time passed since the date of MRI, and $\mathcal{H}_{CG}(\mathbf{x})$ is a Heaviside function with value 1 in the CG and 0 elsewhere. The parameter ϱ adjusts the value of the pressure p_{BPH} to obtain the estimated CG growth rate. Taking all the considerations above, we model prostatic tissue as a linear elastic, heterogeneous, isotropic material whose constitutive equation is given by

$$\boldsymbol{\sigma} = \lambda(\boldsymbol{\nabla}\cdot\mathbf{u})\mathbf{I} + 2\mu\boldsymbol{\nabla}^s\mathbf{u} - \kappa\phi\mathbf{I} - K\varrho\frac{g\Delta t}{V_{MRI}}\mathcal{H}_{CG}(\mathbf{x})\mathbf{I} \quad [10]$$

where $\boldsymbol{\sigma}$ is the stress tensor, λ and μ are the Lamé constants, $\mathbf{u}$ is the displacement vector, and $\mathbf{x}$ is the position vector. The segmentation of CG and PZ was extracted from our patient's imaging data and mapped over the quadrature points to define heterogeneous material properties (see Fig. 1).

We computed tumor volume V_ϕ and serum PSA P as (39):

$$V_\phi = \int_\Omega \phi d\Omega \qquad P = \int_\Omega p d\Omega \quad [11]$$

where Ω is the prostate segmented on the patient's MR images.

Because we are focusing on localized PCa, we imposed zero-valued Dirichlet conditions for ϕ all over the prostate boundary $\partial\Omega$. We set natural boundary conditions for s and p. The confinement of the prostate within the pelvic area (1) was modeled with Winkler boundary conditions on the external surface of the prostate, while free-displacement was enabled along the urethra, i.e.,

$$\begin{aligned} \boldsymbol{\sigma}\mathbf{n} &= -k_w\mathbf{u} \quad \text{in } \partial\Omega|_{exterior} \\ \boldsymbol{\sigma}\mathbf{n} &= \mathbf{0} \quad \text{in } \partial\Omega|_{urethra} \end{aligned} \qquad [12]$$

where $\mathbf{n}$ is the outer normal vector to $\partial\Omega$ and k_w is the Winkler constant.

The initial condition of the phase field, ϕ_0, was an L^2-projection of the tumor segmentation extracted from the patient's T2-weighted MR images and mapped over quadrature points or was artificially modeled with an L^2-projected hyperbolic tangent field. The initial conditions for s and p were approximated with linear functions based on ϕ_0 (40). Linear elasticity allows us to apply the Principle of Superposition and set zero-valued initial conditions for the displacements, i.e., $\mathbf{u}_0 = \mathbf{0}$. This means that we are only computing the displacements produced since the MR date.

To study how BPH mechanically influences PCa growth, we estimated the stress state $\boldsymbol{\sigma}^0$ caused by the history of BPH before the detection of PCa at MR date and leveraged it as a prestress to compute M in Eq. (1). Hence, for this purpose, $\boldsymbol{\sigma} = \boldsymbol{\sigma}^0 + \boldsymbol{\sigma}^1$, where $\boldsymbol{\sigma}^1$ are the stresses developed since the detection of PCa at MR date. To estimate $\boldsymbol{\sigma}^0$, we assumed that the volume of the patient's prostate was 20 cc at age 40 (1, 3) and leveraged Eq. (4) with a negative value for g and $\Delta t = 14$ years to approximate the undeformed, healthy state of our patient's prostate according to the standard anatomical features (1). Because we are using linear elasticity, it suffices to reverse the sign of the obtained displacements to yield $\mathbf{u}^0$ and then approximate $\boldsymbol{\sigma}^0$ as

$$\boldsymbol{\sigma}^0 = \lambda\left(\boldsymbol{\nabla}\cdot\mathbf{u}^0\right)\mathbf{I} + 2\mu\boldsymbol{\nabla}^s\mathbf{u}^0 - K\varrho\frac{g\Delta t^0}{V_{MRI}}\mathcal{H}_{CG}(\mathbf{x})\,\mathbf{I} \qquad [13]$$

where g is now positive and $\Delta t^0 = 14$ years.

Parameter selection for Eq. (1)-Eq. (3) has been previously discussed (39) and it is provided in Table 1. We set the values of the Young modulus of PZ and CG to $E_{PZ} = 3$ KPa and $E_{CG} = 6$ KPa, respectively (42–45). Because living soft tissues have high content of water (34, 37, 42), we set the Poisson coefficients $\nu_{PZ} = \nu_{CG} = 0.40$. We empirically calibrated $\beta_1 = 0.80$ 1/KPa and $\beta_2 = 1.50$ in agreement with the experimental and clinical observations reported in previous studies on tumor growth (23–28, 32–34). We selected $\kappa = 2.50$ KPa to produce displacements in the order of 1 mm. The analysis of BPH and PCa deformation and the computation of the stress fields $\boldsymbol{\sigma}^0$ rendered $g = 2.34$ cc/year, $\varrho = 2.78$, and $k_w = 0.23$ KPa/mm. These values for g and ϱ reasonably agree with previous observations in the literature for our patient characteristics (1, 3, 50, 52–54).

Table 1. List of parameters in Eq. (1)**-**Eq. (3)**.**

Parameter	Notation	Value
Diffusivity of the phase field	D_ϕ	200 mm^2/year
Time scale for the phase field	τ	0.01 years
Nutrient-induced tumor growth rate	χ	600 L/(g·year)
Apoptosis rate	A	600 1/year
Nutrient diffusivity	D_s	$5.47\cdot10^3$ mm^2/year
Nutrient supply	S	2.70 g/(L·day)
Nutrient consumption rate	δ	2.75 g/(L·day)
Nutrient natural decay rate	γ_s	1000 1/year
Tissue PSA diffusivity	D_p	200 mm^2/year
Healthy tissue PSA production rate	α_h	6.25 (ng/mL)/(cc·year)
Tumoral tissue PSA production rate	α_c	$\alpha_c = 15\alpha_h$
Tissue PSA natural decay rate	γ_p	100 1/year

Numerical methods. Since tumor growth and BPH are modeled as quasistatic processes, we adopted a staggered approach to solve the equations in our mathematical model. We calculated tumor growth at every time step, but we only updated the displacements every two time steps. We performed spatial discretization by means of a standard isogeometric Bubnov-Galerkin approach using a three-dimensional C^1 quadratic Non-Uniform Rational B-spline (NURBS) space (39, 40, 59–61). Temporal integration in the tumor growth problem was carried out with the generalized-α method (62, 63). This technique led to a nonlinear problem in each time step, which we linearized using the Newton-Raphson method. The resulting linear system was solved utilizing the GMRES algorithm (64) with a diagonal preconditioner. We also used the preconditioned GMRES to solve the quasistatic elastic problem. We chose a constant time step of 0.002 years and the parameters in the generalized-α method were set as in previous studies (40, 65).

Construction of the prostate mesh. Multiple methodologies permit the construction of solid anatomic NURBS models (66, 67). Because the geometries of the prostate and a solid torus are topologically equivalent, we leveraged a parametric mapping algorithm (68, 69) to deform a torus solid NURBS model to match with a patient-specific prostate surface model. We used 3DSlicer (70) to generate a triangular surface model of the prostate from the contours of the organ and the urethra drawn on the T2-weighted MR images, using the provided prostate segmentation as guidance. The resulting surface was smoothed in MeshLab (71).

The original torus and prostate NURBS meshes were discretised with 32x32x8 elements along the toroidal direction, the cross-section circumferential direction, and the cross-section radial direction, respectively. We globally refined the prostate mesh to a 256x256x64 elements using standard knot insertion (60) to perform our simulations with a good level of accuracy.

ACKNOWLEDGMENTS. G.L., P.D.F., and H.G. were partially supported by the European Research Council (Contract 307201) and Xunta de Galicia (Consellería de Cultura, Educación e Ordenación Universitaria). G.L. and A.R. were partially supported by Fondazione Cariplo - Regione Lombardia through the project "Verso nuovi strumenti di simulazione super veloci ed accurati basati sull'analisi isogeometrica", within the program RST - rafforzamento. The authors thank Pablo Orosa-Iglesias (Universidade da Coruña, Spain) for his valuable help in the construction of the prostate mesh. The authors acknowledge the Centro de Supercomputación de Galicia (Santiago de Compostela, Spain) for providing HPC resources that contributed to the results presented in this paper.

1. Wein AJ, Kavoussi LR, Novick AC, Partin AW, Peters CA (2012) *Campbell-Walsh Urology: Expert Consult Premium Edition: Enhanced Online Features and Print, 4-Volume Set.* (Elsevier Saunders), 10th edition.
2. Ferlay J, et al. (2015) Cancer incidence and mortality worldwide: Sources, methods and major patterns in GLOBOCAN 2012. *International Journal of Cancer* 136(5):E359–E386.
3. Berry SJ, Coffey DS, Walsh PC, Ewing LL (1984) The development of human benign prostatic hyperplasia with age. *The Journal of Urology* 132(3):474 – 479.
4. Coakley FV, Hricak H (2000) Radiologic anatomy of the prostate gland: a clinical approach. *Radiologic Clinics of North America* 38(1):15–30.
5. Villeirs GM, L.Verstraete K, Neve WJD, Meerleer GOD (2005) Magnetic resonance imaging anatomy of the prostate and periprostatic area: a guide for radiotherapists. *Radiotherapy and Oncology* 76(1):99 – 106.
6. De Visschere PJ, et al. (2017) Multiparametric magnetic resonance imaging characteristics of normal, benign and malignant conditions in the prostate. *European Radiology* 27(5):2095–2109.
7. Noworolski SM, Vigneron DB, Chen AP, Kurhanewicz J (2008) Dynamic contrast-enhanced MRI and MR diffusion imaging to distinguish between glandular and stromal prostatic tissues. *Magnetic Resonance Imaging* 26(8):1071 – 1080.
8. Alcaraz A, Hammerer P, Tubaro A, Schröder FH, Castro R (2009) Is there evidence of a relationship between benign prostatic hyperplasia and prostate cancer? Findings of a literature review. *European Urology* 55(4):864 – 875.
9. Ørsted DD, Bojesen SE (2013) The link between benign prostatic hyperplasia and prostate cancer. *Nature Reviews Urology* 10(1):49–54.
10. Chen ME, Troncoso P, Johnston D, Tang K, Babaian RJ (1999) Prostate cancer detection: relationship to prostate size. *Urology* 53(4):764–768.
11. Werahera PN, et al. (2012) Optimization of prostate cancer diagnosis by increasing the number of core biopsies based on gland volume. *International Journal of Clinical and Experimental Pathology* 5(9):892.
12. de Gorski A, et al. (2015) Accuracy of magnetic resonance imaging/ultrasound fusion targeted biopsies to diagnose clinically significant prostate cancer in enlarged compared to smaller prostates. *The Journal of Urology* 194(3):669–673.
13. Ung JO, San Francisco IF, Regan MM, DeWolf WC, Olumi AF (2003) The relationship of prostate gland volume to extended needle biopsy on prostate cancer detection. *The Journal of Urology* 169(1):130–135.

14. Kulkarni GS, et al. (2006) Evidence for a biopsy derived grade artifact among larger prostate glands. *The Journal of Urology* 175(2):505–509.
15. Diaz AW, et al. (2013) Can magnetic resonance-ultrasound fusion biopsy improve cancer detection in enlarged prostates? *The Journal of Urology* 190(6):2020–2025.
16. Scattoni V, et al. (2008) Initial extended transrectal prostate biopsy-are more prostate cancers detected with 18 cores than with 12 cores? *The Journal of Urology* 179(4):1327–1331.
17. Freedland SJ, et al. (2005) Prostate size and risk of high-grade, advanced prostate cancer and biochemical progression after radical prostatectomy: a search database study. *Journal of Clinical Oncology* 23(30):7546–7554.
18. Kassouf W, et al. (2007) Effect of prostate volume on tumor grade in patients undergoing radical prostatectomy in the era of extended prostatic biopsies. *The Journal of Urology* 178(1):111 – 114.
19. Briganti A, et al. (2007) Prostate volume and adverse prostate cancer features: fact not artifact. *European Journal of Cancer* 43(18):2669–2677.
20. Newton MR, et al. (2010) Smaller prostate size predicts high grade prostate cancer at final pathology. *The Journal of Urology* 184(3):930–937.
21. Hong SK, Poon BY, Sjoberg DD, Scardino PT, Eastham JA (2014) Prostate size and adverse pathologic features in men undergoing radical prostatectomy. *Urology* 84(1):153–157.
22. Gordon V, et al. (2003) Measuring the mechanical stress induced by an expanding multicellular tumor system: a case study. *Experimental Cell Research* 289(1):58 – 66.
23. Stylianopoulos T, et al. (2013) Coevolution of solid stress and interstitial fluid pressure in tumors during progression: Implications for vascular collapse. *Cancer Research* 73(13):3833–3841.
24. Jain RK, Martin JD, Stylianopoulos T (2014) The role of mechanical forces in tumor growth and therapy. *Annual Review of Biomedical Engineering* 16(1):321–346.
25. Helmlinger G, Netti PA, Lichtenbeld HC, Melder RJ, Jain RK (1997) Solid stress inhibits the growth of multicellular tumor spheroids. *Nature Biotechnology* 15(8):778–783.
26. Roose T, Netti PA, Munn LL, Boucher Y, Jain RK (2003) Solid stress generated by spheroid growth estimated using a linear poroelasticity model. *Microvascular Research* 66(3):204 – 212.
27. Cheng G, Tse J, Jain RK, Munn LL (2009) Micro-environmental mechanical stress controls tumor spheroid size and morphology by suppressing proliferation and inducing apoptosis in cancer cells. *PLOS ONE* 4(2):1–11.
28. Voutouri C, Mpekris F, Papageorgis P, Odysseos AD, Stylianopoulos T (2014) Role of constitutive behavior and tumor-host mechanical interactions in the state of stress and growth of solid tumors. *PLOS ONE* 9(8):1–9.
29. Anderson AR, Quaranta V (2008) Integrative mathematical oncology. *Nature Reviews. Cancer* 8(3):227–234.
30. Yankeelov TE, et al. (2013) Clinically relevant modeling of tumor growth and treatment response. *Science Translational Medicine* 5(187):187ps9.
31. Oden JT, et al. (2016) Toward predictive multiscale modeling of vascular tumor growth. *Archives of Computational Methods in Engineering* 23(4):735–779.
32. Weis JA, et al. (2015) Predicting the response of breast cancer to neoadjuvant therapy using a mechanically coupled reaction–diffusion model. *Cancer Research* 75(22):4697–4707.
33. Lima E, et al. (2017) Selection and validation of predictive models of radiation effects on tumor growth based on noninvasive imaging data. *Computer Methods in Applied Mechanics and Engineering* 327:277 – 305.
34. Weis JA, Miga MI, Yankeelov TE (2017) Three-dimensional image-based mechanical modeling for predicting the response of breast cancer to neoadjuvant therapy. *Computer Methods in Applied Mechanics and Engineering* 314:494 – 512.
35. Chen X, Summers RM, Yao J (2013) Kidney tumor growth prediction by coupling reaction-diffusion and biomechanical model. *IEEE Transactions on Biomedical Engineering* 60(1):169–173.
36. Liu Y, et al. (2014) Patient specific tumor growth prediction using multimodal images. *Medical Image Analysis* 18(3):555 – 566.
37. Clatz O, et al. (2005) Realistic simulation of the 3-D growth of brain tumors in MR images coupling diffusion with biomechanical deformation. *IEEE Transactions on Medical Imaging* 24(10):1334–1346.
38. Hogea C, Davatzikos C, Biros G (2008) An image-driven parameter estimation problem for a reaction–diffusion glioma growth model with mass effects. *Journal of Mathematical Biology* 56(6):793–825.
39. Lorenzo G, et al. (2016) Tissue-scale, personalized modeling and simulation of prostate cancer growth. *Proceedings of the National Academy of Sciences of the United States of America* 113(48):E7663–E7671.
40. Lorenzo G, Scott M, Tew K, Hughes T, Gomez H (2017) Hierarchically refined and coarsened splines for moving interface problems, with particular application to phase-field models of prostate tumor growth. *Computer Methods in Applied Mechanics and Engineering* 319:515 – 548.
41. Qin RS, Bhadeshia HK (2010) Phase field method. *Materials Science and Technology* 26(7):803–811.
42. Bharatha A, et al. (2001) Evaluation of three-dimensional finite element-based deformable registration of pre- and intraoperative prostate imaging. *Medical Physics* 28(12):2551–2560.
43. Zhai L, et al. (2010) Characterizing stiffness of human prostates using acoustic radiation force. *Ultrasonic Imaging* 32(4):201–213.
44. Wang Y, et al. (2016) Patient-specific deformation modelling via elastography: application to image-guided prostate interventions. *Scientific Reports* 6:27386.
45. Rouvière O, et al. (2017) Stiffness of benign and malignant prostate tissue measured by shear-wave elastography: a preliminary study. *European Radiology* 27(5):1858–1866.
46. Irgens F (2008) *Continuum Mechanics*. (Springer).
47. Partin AW, et al. (1990) Prostate specific antigen in the staging of localized prostate cancer: Influence of tumor differentiation, tumor volume and benign hyperplasia. *The Journal of Urology* 143(4):747 – 752.
48. Turkbey B, et al. (2012) Correlation of magnetic resonance imaging tumor volume with histopathology. *The Journal of Urology* 188(4):1157 – 1163.
49. Thompson IM, et al. (2003) The influence of finasteride on the development of prostate cancer. *New England Journal of Medicine* 349(3):215–224.
50. Cao N, et al. (2017) The characteristics of the transitional zone in prostate growth with age. *Urology* 105:136 – 140.
51. Rusu M, et al. (2017) Computational imaging reveals shape differences between normal and malignant prostates on MRI. *Scientific Reports* 7:41261.
52. Lieber MM, et al. (2010) Natural history of benign prostatic enlargement: long-term longitudinal population-based study of prostate volume doubling times. *BJU International* 105(2):214–219.
53. Roehrborn CG, et al. (2000) Serum prostate specific antigen is a strong predictor of future prostate growth in men with benign prostatic hyperplasia. *The Journal of Urology* 163(1):13–20.
54. Williams AM, et al. (1999) Prostatic growth rate determined from MRI data: Age-related longitudinal changes. *Journal of Andrology* 20(4):474–480.
55. Goriely A (2017) *The Mathematics and Mechanics of Biological Growth (Interdisciplinary Applied Mathematics)*. (Springer).
56. Menzel A, Kuhl E (2012) Frontiers in growth and remodeling. *Mechanics Research Communications* 42:1 – 14.
57. Lemaître G, et al. (2015) Computer-Aided Detection and diagnosis for prostate cancer based on mono and multi-parametric MRI: A review. *Computers in Biology and Medicine* 60:8 – 31.
58. Lemaître G (2016) Ph.D. thesis (Universitat de Girona and Université de Bourgogne).
59. Hughes T, Cottrell J, Bazilevs Y (2005) Isogeometric analysis: CAD, finite elements, NURBS, exact geometry and mesh refinement. *Computer Methods in Applied Mechanics and Engineering* 194(39-41):4135–4195.
60. Cottrell JA, Hughes TJ, Bazilevs Y (2009) *Isogeometric Analysis: Toward Integration of CAD and FEA*. (Wiley).
61. Piegl LA, Tiller W (1996) *The NURBS Book (Monographs in Visual Communication)*. (Springer).
62. Chung J, Hulbert G (1993) A time integration algorithm for structural dynamics with improved numerical dissipation: the generalized-α method. *Journal of Applied Mechanics* 60(2):371–375.
63. Jansen KE, Whiting CH, Hulbert GM (2000) A generalized-α method for integrating the filtered Navier–Stokes equations with a stabilized finite element method. *Computer Methods in Applied Mechanics and Engineering* 190(3–4):305–319.
64. Saad Y, Schultz MH (1986) GMRES: A Generalized Minimal Residual Algorithm for Solving Nonsymmetric Linear Systems. *SIAM Journal on Scientific and Statistical Computing* 7(3):856–869.
65. Gómez H, Calo VM, Bazilevs Y, Hughes TJ (2008) Isogeometric analysis of the Cahn-Hilliard phase-field model. *Computer Methods in Applied Mechanics and Engineering* 197(49-50):4333–4352.
66. Zhang YJ (2016) *Geometric Modeling and Mesh Generation from Scanned Images (Chapman & Hall/CRC Mathematical and Computational Imaging Sciences Series)*. (Chapman and Hall/CRC).
67. Zhang Y, Bazilevs Y, Goswami S, Bajaj CL, Hughes TJ (2007) Patient-specific vascular NURBS modeling for isogeometric analysis of blood flow. *Computer Methods in Applied Mechanics and Engineering* 196(29-30):2943–2959.
68. Floater MS, Hormann K (2005) Surface Parameterization: a Tutorial and Survey in *Advances in Multiresolution for Geometric Modelling*, eds. Dodgson NA, Floater MS, Sabin MA. (Springer Berlin Heidelberg, Berlin, Heidelberg), pp. 157–186.
69. Zhang Y, Wang W, Hughes TJ (2012) Solid T-spline construction from boundary representations for genus-zero geometry. *Computer Methods in Applied Mechanics and Engineering* 249:185 – 197.
70. Fedorov A, et al. (2012) 3D Slicer as an image computing platform for the Quantitative Imaging Network. *Magnetic Resonance Imaging* 30(9):1323 – 1341.
71. Cignoni P, et al. (2008) MeshLab: an Open-Source Mesh Processing Tool in *Eurographics Italian Chapter Conference*, eds. Scarano V, Chiara RD, Erra U. (The Eurographics Association).